JOURNAL OF SYNCHROTRON RADIATION
ISSN 1600-5775

Eyeing the past: synchrotron μ-XANES and XRF imaging of tarnish distribution on 19th century daguerreotypes

M. S. Kozachuk,[a] T. K. Sham,[a]* R. R. Martin,[a] A. J. Nelson[a,b] and I. Coulthard[c]

[a]The Department of Chemistry, The University of Western Ontario, 1151 Richmond Street, London, Ontario N6A 5B7, Canada, [b]The Department of Anthropology, The University of Western Ontario, 1151 Richmond Street, London, Ontario N6A 5B7, Canada, and [c]Canadian Light Source Inc., 44 Innovation Boulevard, Saskatoon, Saskatchewan S7N 2V3, Canada. *Correspondence e-mail: tsham@uwo.ca

Received 7 February 2019
Accepted 3 May 2019

Edited by P. A. Pianetta, SLAC National Accelerator Laboratory, USA

Keywords: synchrotron X-ray fluorescence imaging; daguerreotypes; absorption spectroscopy; scanning electron microscopy; surface analysis; tarnish; degradation compounds.

Louis-Jacques-Mandé Daguerre introduced the first successful photographic process, the daguerreotype, in 1839. Tarnished regions on daguerreotypes supplied by the National Gallery of Canada were examined using scanning electron microscopy energy-dispersive X-ray spectroscopy and synchrotron-radiation analysis. Synchrotron X-ray fluorescence imaging visualized the distribution of sulfur and chlorine, two primary tarnish contributors, and showed that they were associated with the distribution of image particles on the surface. X-ray absorption near-edge structure spectroscopy determined the tarnish to be primarily composed of AgCl and Ag_2S. Au_2S, Au_2SO_4, $HAuCl_4$ and $HgSO_4$ were also observed to be minor contributors. Environmental contamination may be a source of these degradation compounds. Implications of these findings will be discussed.

1. Introduction

Louis-Jacques-Mandé Daguerre introduced the daguerreotype, the first successful photographic technique, in 1839 (Arago, 1839). While the next 25 years saw advances on Daguerre's original method, the daguerreotype was soon surpassed by other photographic techniques (Ravines *et al.*, 2016*a*). Daguerre's original procedure involved rendering a highly polished silver-coated copper plate, photosensitive by exposure to iodine vapour. Photolysis of this silver halide layer leads to the production of silver image particles that are subsequently fixed with mercury vapour. Excess halide is removed with a thiosulfate solution (Da Silva *et al.*, 2010). Once completed, the image is placed in a protective case, which includes the plate, a mat (usually stamped brass) and a glass cover (Barger *et al.*, 1989). Later improvements to Daguerre's process included the use of chlorine and bromine in the sensitizing step, thus reducing the exposure time to a few seconds, and a gilding step using a gold(III) chloride thiosulfate solution (Ravines *et al.*, 2016*b*). This later process increased the brilliance, contrast and durability of the image (Ravines *et al.*, 2016*a*).

The appearance of the daguerreotype is produced by the scattering of light from the plate and the image particles on the surface (Ravines *et al.*, 2016*a*). The density of image particles (defined as the number of image particles per unit area) is proportional to the intensity of the incident light: high intensity produces high particle densities ($\sim 2 \times 10^5$ particles mm^{-2}) and low intensity yields low particle densities (<100 particles mm^{-2}) (Barger & White, 1991). This variation

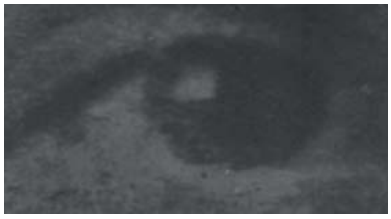

of image-particle density produces the range of grey tones that typify the daguerreotype.

Daguerreotypes are prone to tarnish, such as silver chloride, silver oxides and sulfides; copper sulfides and chlorides have also been reported (Barger *et al.*, 1982*a*,*b*; Ravines *et al.*, 2008; Ravines, 2010; Anglos *et al.*, 2002; Hogan *et al.*, 1999; Centeno *et al.*, 2011; Lavédrine *et al.*, 2009). Recently, synchrotron radiation, a non-contact, non-invasive and non-destructive technique, has been used to study the elemental distribution and chemistry both of the surface and with depth (Kozachuk *et al.*, 2017*a*,*b*). Paired with scanning electron microscopy, the information attained can not only provide insights into the cause(s) of the tarnish but can also suggest improved conservation and/or restoration methods.

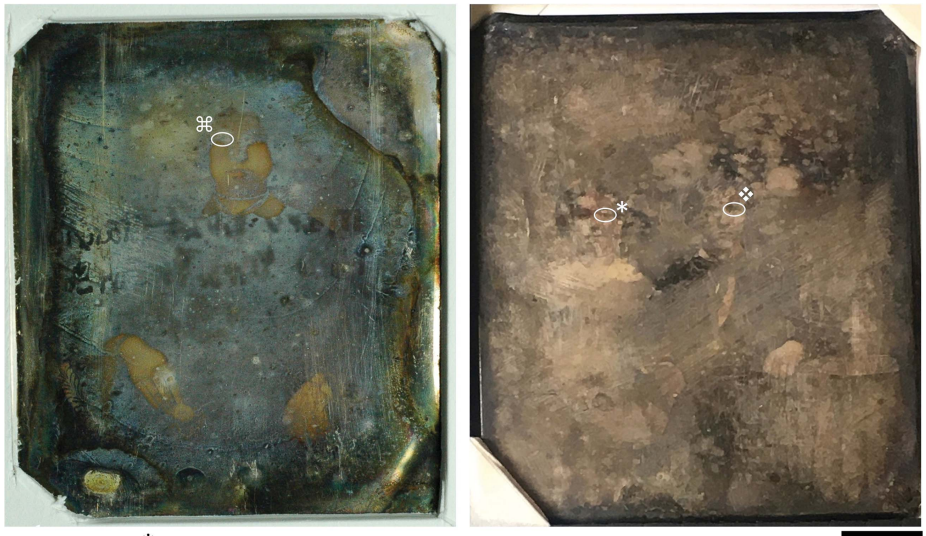

Figure 1
Daguerreotypes of (*a*) an unidentified woman (conservation study collection) and (*b*) an unidentified man and woman (accession number PSC70:112) both from the NGC, *ca*. 1850s. Areas examined with SEM–EDX and synchrotron-radiation XRF are marked.

To establish effective and safe cleaning methods for these silver images, a greater understanding of the chemical nature and distribution of these corrosion and decomposition compounds is required. The purpose of this work is to examine the distribution and speciation of tarnish on the surface of two 19th century daguerreotypes, supplied by the National Gallery of Canada (NGC, Ottawa, Canada). Scanning electron microscopy energy-dispersive X-ray (SEM–EDX) spectroscopy and synchrotron-radiation analysis techniques including X-ray fluorescence (XRF) imaging and X-ray absorption near-edge structure (XANES) spectroscopy were used. These are ideal complementary techniques to study the surface morphology, element distribution and chemistry of daguerreotypes with special attention to tarnished regions. Synchrotron-based XRF microscopy images the distribution of tarnish across the daguerreotype surface and XANES allows for the characterization of the chemical environment of the degradation at specific locations. SEM–EDX was used to track the morphology and the preferential dissemination of the tarnish.

2. Materials and methods

2.1. Sample materials

Two daguerreotypes, one of an unidentified woman and another of an unidentified man and woman (Fig. 1), were supplied by the NGC. Both images have substantial surface tarnish appearing as a white haze covering the image. No sample preparation was conducted prior to the analysis. The eye regions on both plates were chosen for the analysis since they contain a large range of grey tones typical of daguerreotypes within a relatively small area.

2.2. Surface characterization

2.2.1. Synchrotron-radiation analysis. XRF imaging was conducted at the Canadian Light Source (CLS), Saskatoon, Saskatchewan, with the medium energy X-ray microprobe endstation, SXRMB (06B1-1). Both two-dimensional XRF maps and XANES spectra were collected at this beamline (Hu *et al.*, 2010). A Si(111) double-crystal monochromator and Kirkpatrick–Baez (KB) micro-focusing mirrors achieved a beam size of ∼10 µm. The sample stage is housed in a separate chamber downstream, equipped with a Bruker four-element Si(Li) drift detector, a CCD camera and a three-axis (*X*, *Y* and *Z*) sample stage. Between the KB mirrors and the sample compartment, a micro-ion chamber is positioned for beam alignment and monitoring I_0. The spot size of the beam at the specimen was ∼10 µm × 10 µm at an incident energy of 3950 eV, which is above the Ag $L_{3,2}$-edge (3351 eV and 3524 eV, respectively), the S *K*-edge (2472 eV) and the Cl *K*-edge (2822 eV).

Silver (Ag), chlorine (Cl) and sulfur (S) XANES were collected in partial fluorescence yield (FLY) mode. The parameters of the scans are presented in Table 1. A series of standard XANES spectra were collected (Table 2) as representative compounds likely to contribute to surface contamination including possible formations of Ag–Au amalgams (presented in atomic percent). XRF images for Ag, Cl and S are the focus of this study.

2.2.2. Synchrotron data processing. All XANES spectra were analyzed using the *Athena* software package (Ravel & Newville, 2005). After background subtraction, normalization (edge-jump normalized to unity) and spectrum averaging, all spectra were calibrated following the procedure outlined by Ravel (2009). When appropriate, linear combination fit (LCF)

Table 1
Outline of X-ray absorption spectroscopy parameters for Ag, S and Cl collected at the SXRMB beamline at the Canadian Light Source.

Element of interest	Energy range	Energetic step size (pre-edge)	Energetic step size (at the edge)	Energetic step size (post-edge)	Dwell time (s)	Edge-jump analyzed
Ag	3320–3450 eV	2.00 eV	0.15 eV	0.75 eV	1	L_3-edge (3351 eV)
S	2442–2572 eV	2.00 eV	0.20 eV	0.75 eV	4	*K*-edge (2472 eV)
Cl	2800–2950 eV	2.00 eV	0.15 eV	0.75 eV	4	*K*-edge (2822 eV)

Table 2
List of standards used for XANES analysis.

Element of interest	Standard(s) examined	Edge analyzed
Ag	Ag, $Ag_{95}Au_5$, $Ag_{75}Au_{25}$, AgI, AgCl, AgBr, Ag_2O, Ag_2S, $AgNO_3$	L_3-edge
Cl	AgCl, NaCl, KCl, $HgCl_2$, $HAuCl_4$, $AuCl_3$	*K*-edge
S	Ag_2S, Na_2SO_4, Na_2SO_3, CuS, Cu_2S, $HgSO_4$, HgS, $Na_2S_2O_3{\cdot}5H_2O$, Au_2S, Au_2SO_4	*K*-edge

analyses were performed on normalized spectra. As such, a LCF models a spectrum of unknown composition using a series of reference spectra; the number of reference spectra required depends on the complexity of the system (*i.e.* more reference spectra are needed to model a complex system). Each standard spectrum is interpolated onto the energy grid of the unknown spectrum over an energy range of −20 eV to +30 eV of the threshold (E_0). Goodness of fit is estimated by taking the difference between the collected spectrum and the fitted spectrum. Extra caution was taken for photon-energy calibration using standards.

X-ray fluorescence maps were created using the partial FLY of the element of interest [*e.g.* Ag *Lα* (2984 eV), S *Kα* (2307 eV) and Cl *Kα* (2622 eV) X-ray emission, for the Ag, S and Cl maps, respectively] normalized to I_0 (the intensity of the exciting X-ray), and analyzed using the *SMAK* software program (Webb *et al.*, 2011).

2.2.3. SEM–EDX. Scanning electron microscopy images from both daguerreotype plates were examined with the LEO (Zeiss) 1540XB FIB/SEM instrument at the Western Nanofabrication Facility. Topographic imaging was performed at 1 kV with a working distance of 4 mm, and backscatter imaging was performed at 10 kV and 9 mm. An Oxford Instruments X-max 50 detector was used for EDX spectroscopy, and analysis was performed with *INCA* analysis software (INCA, 2016).

3. Results

3.1. SEM–EDX analysis

The region of the woman's eye [Fig. 1(*b*)] used in this portion of the SEM analysis is shown in Fig. 2, and detailed SEM images of the particle distribution between the highlight and shadow regions are shown in Fig. 3 (Barger & White, 1991). Examples of a size, shape and distribution typical of a tarnished highlight and a shadow region are provided in Figs. 3(*a*)–3(*c*). The boundary between these two regions is shown clearly with a dashed line in Fig. 3(*d*). SEM–EDX maps were obtained from the border of the blemish region [note the EDX label in Fig. 3(*a*)] and are shown in Fig. 4, which shows the presence of C, Cu and O. The C and O are indicative of organic contamination while the Cu may be assigned to diffusion from the underlying plate through grain boundaries and/or at edges of the daguerreotype (Marquis *et al.*, 2015), though this diffusion mechanism has been questioned (Robinson, 2017). Simple thinning of the Ag overlayer during sample preparation cannot be excluded along with the dete-

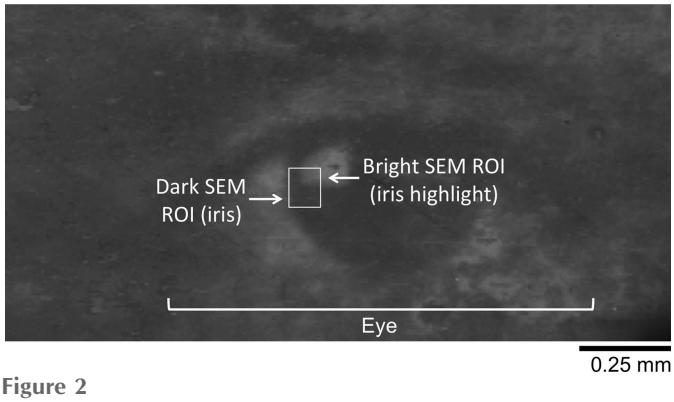

Figure 2
SEM image of the woman's eye on daguerreotype PSC 70:112 [Fig. 1(*b*)] with the SEM region of interest (ROI) indicated.

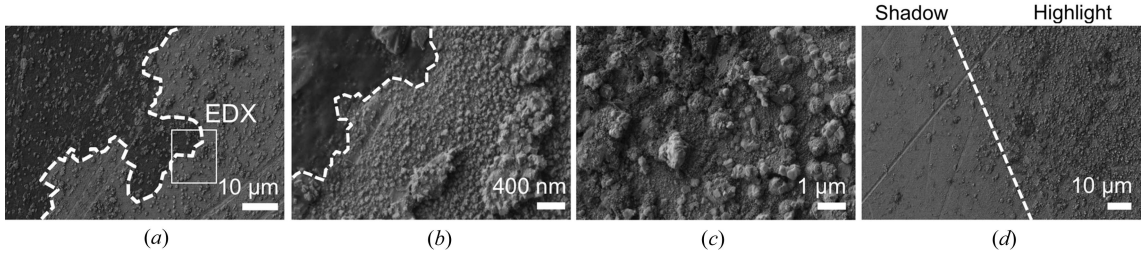

Figure 3
SEM images collected from daguerreotype PSC70:112 [Fig. 1(*b*)] within the ROI indicated in Fig. 2. (*a*) General shadow region with surface tarnish; the location of EDX (shown in Fig. 4) examination is outlined. (*b*) High magnification of shadow region. (*c*) High magnification of highlight area. (*d*) Transition between highlight and shadow regions.

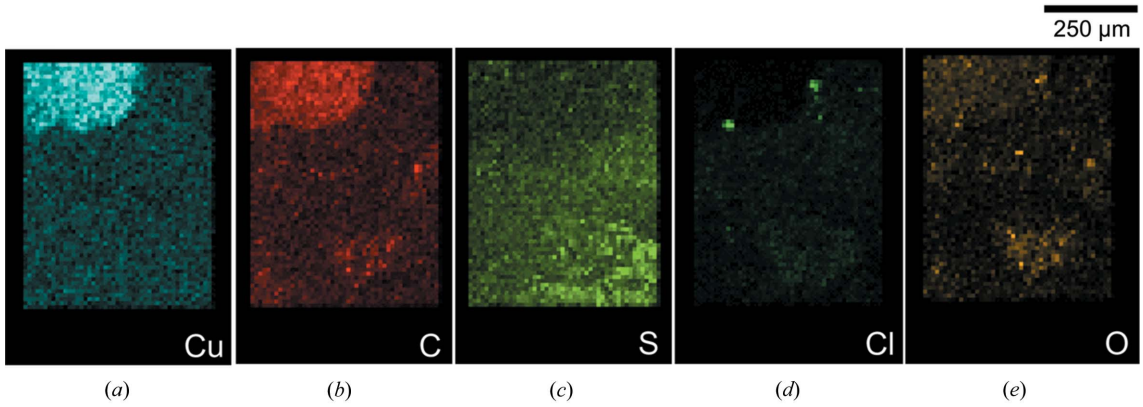

Figure 4
SEM–EDX of tarnished surface with the ROI indicated by the rectangle in Fig. 3(*a*). Brightest colour intensity indicates the relative concentration maximum for each element and black correlates to the relative minimum elemental concentration.

rioration of the cover glass, which has been shown to produce Cu deposits on the surface (Barger *et al.*, 1989).

3.2. Synchrotron XRF and µ-XANES analysis

X-ray fluorescence images of the man's right eye [Fig. 1(*b*)] are shown in Fig. 5. Like in the EDX Ag map, excitation above the Ag *L*-edge excites the image particle as well as the bulk of the plate. The production of a detailed image is due to the image particles on the surface and the shallow penetration depth of the soft X-ray. In the Ag XRF image, regions of low image-particle density correlate with the greatest Ag fluorescence signal. For example, the iris of the eye, which is represented by dark red on the colour scale, is a region of low image-particle density. Conversely, regions of high image-particle density, such as the highlight of the eye, have a decreased Ag fluorescence signal (~10%). This reduction in detected Ag fluorescence signal in high particle-density areas is most likely to be due to the overlayer of polluting elements (AgCl and/or Ag_2S) and/or from an enhanced overlayer of Au, a result of the gilding process.

The S XRF map (Fig. 5) shows a non-uniform distribution of S signal, which is a common morphological characteristic of the sulfidation of Ag (Graedel, 1992). Similarly, the Cl fluorescence signal follows an indistinct, random distribution across the eye region.

The chemical environment was examined with XANES. At all three locations where the S *K*-edge XANES was collected (Fig. 5), the primary feature is observed at 2473 eV, which arises from a $1s \rightarrow 3p$ transition. The location of this first transition suggests that the S $p\pi^*$ orbital is directly involved in a covalent Ag–S interaction (Solomon *et al.*, 2003) and is seen as the double feature of the first peak (indicated by arrows at this feature in spectrum S1, Fig. 5), indicating the dominance of Ag_2S at all sites (Solomon *et al.*, 2003). This was supported with LCFs (Table 3). The second peak at about 2482 eV corresponds to an oxidized form of S where the oscillation is characteristic of σ^* multiple scattering in a t_d environment (Manceau & Nagy, 2012). These two observations suggest a mixture of S compounds at the surface.

The Cl *K*-edge (Fig. 5), which represents the excitation of an electron from a 1*s* orbital to a previously unoccupied 3*p* orbital, has a threshold located at 2822 eV. Examination of the edge-jump location and post-edge

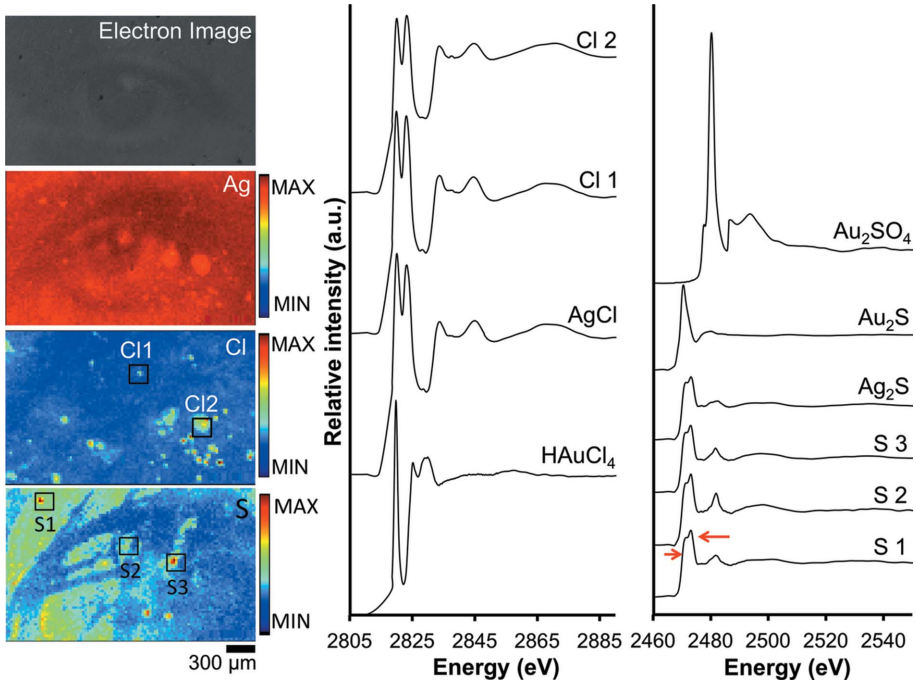

Figure 5
Synchrotron XRF maps from daguerreotype PSC70:112 [Fig. 1(*b*)] of Ag, Cl and S with corresponding XANES for S and Cl *K*-edges shown on the right.

Table 3
LCF results for all sulfur *K*-edge spectra.

Figure	Au_2S (wt%)	Au_2SO_4 (wt%)	Ag_2S (wt%)	$HgSO_4$ (wt%)
Fig. 6, 70:112 hotspot eye centre (S1)	5.30	—	94.7	—
Fig. 6, 70:112 right of eye (S2)	2.50	—	97.5	—
Fig. 6, 70:112 right of eye (S3)	9.50	—	90.5	—
Fig. 7, NGC centre of eye (S1)	—	—	97.4	2.60
Fig. 7, NGC outside of eye (S2)	—	11.9	88.1	—

oscillations indicate that AgCl was the dominant contributor and aligns with the LCF analysis.

The distribution of Ag, S and Cl on the woman's right eye from the NGC study collection plate was also examined (Fig. 6). Here, like in Fig. 5, the Ag XRF shows a relatively greater amount of Ag fluorescence signal from regions with few to no image particles and a relatively lower XRF signal in areas with high image-particle density. The details of the eye can also be observed in the S XRF image as the distribution of S follows the location of the image particles. For instance, in the highlight region of the eye, which would appear as a bright/white tone when viewed optically, a relative increase in S concentration is observed. A light outline of the eye is noted in the Cl XRF image but not with the same clarity as in the Ag or S maps.

Absorption spectra for each element were collected at different regions within the eye. The Ag L_3-edge XANES (edge-jump located at 3351 eV) represents the excitation of a $2p_{3/2}$ electron to unoccupied *s*–*d* bands above the Fermi level (Fig. 6). The lack of a sharp rising edge indicates that the *d*-band is full, like that of pure Ag. Subsequent oscillations arise from the multiple and single scattering of the photoelectrons by the neighbouring atoms. Examination of the highlight region (Fig. 6, spectrum Ag1) is consistent with $Ag_{95}Au_5$ and Ag, indicating a minimal alloying between Au and Ag in the highlight region. LCF analysis of the dark region (spectrum Ag2) shows the major contributors to be $Ag_{95}Au_5$ and $Ag_{75}Au_{25}$, suggesting a greater degree of alloying in the shadow location of the eye. This aligns with previous work (Kozachuk *et al.*, 2017*a*) that determined that dark regions of the plate have relatively less Au on the surface but a greater degree of alloying in the subsurface, while the bright areas have a relatively greater concentration of Au on the surface with minimal alloying below the surface.

An example of the linear combination fitting (Fig. 7) used to semi-quantitatively analyze all XANES spectra is shown for each absorption edge in Fig. 6. The experimental spectra are shown along with the LCF and difference (Diff.) spectra. This does not provide a quantitative error measurement but instead communicates the goodness-of-fit for the unique model applied to each experimental spectrum.

The Cl *K*-edge was collected at three different locations. Spectrum Cl1 is associated with the white of the eye (like Ag1), spectrum Cl2 corresponds to the iris (like Ag2) and spectrum Cl3 represents a midtone region collected at the inner portion of the eye. For all locations, the location of the edge-jump (2822 eV) and the subsequent oscillations match those of the AgCl reference and are confirmed by LCF analysis.

Two S *K*-edge spectra were collected from a highlight (S1) and shadow (S2) region, both of which show the presence of both sulfide and sulfate compounds. While LCF analysis suggests the presence of Hg and Au bonded to an oxidized S species, an Ag-bound sulfate is most likely.

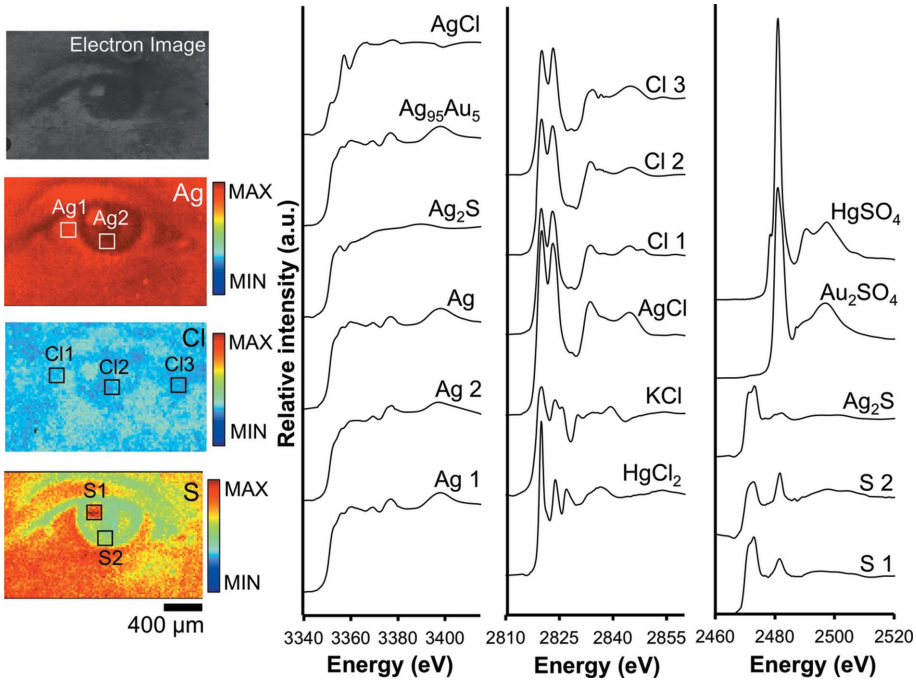

Figure 6
Synchrotron XRF maps for Ag, Cl and S from the NGC study collection plate [Fig. 1(*a*)]. Accompanying XANES spectra for each element are shown to the right of their respective XRF images. Cl1 and Ag1 were collected from the same area and Cl2, Ag2 and S2 were taken at the same location.

4. Discussion of possible tarnishing processes

4.1. Sample selection

While previous studies have used artificially tarnished samples to characterize degradation products on the daguerreotype surface, these models are not necessarily representative of natural tarnishing layers (Da Silva *et al.*, 2010; Marquis *et al.*, 2015; Storme *et*

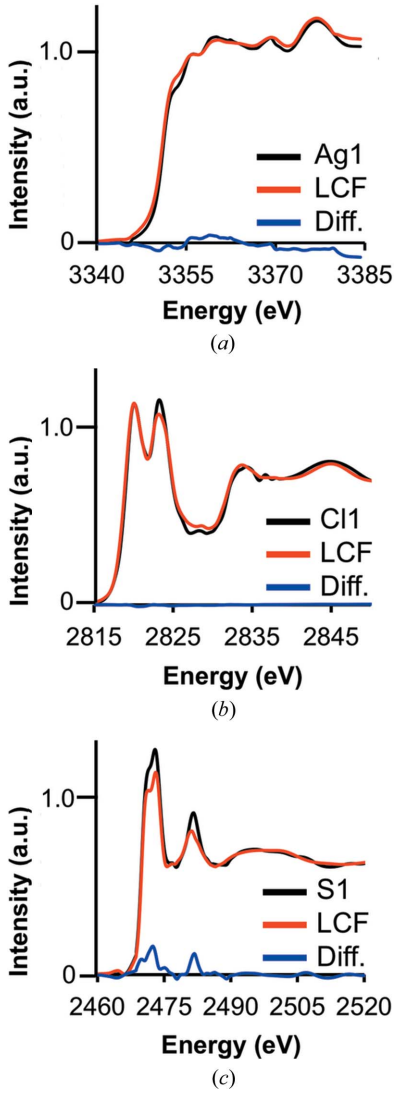

Figure 7
(*a*) Ag L_3-edge (spectrum Ag1), (*b*) Cl *K*-edge (spectrum Cl1) and (*c*) S *K*-edge (spectrum S1) from Fig. 6, with LCF and difference (Diff.) spectra for each absorption edge.

al., 2015). Moreover, artificial ageing in natural environmental conditions often produce inconsistent results that cannot be quantified (Ravines *et al.*, 2008). For instance, morphology, microstructure and composition of the corrosion may depend on the artificial corrosion method used. Furthermore, it is not possible to assume that natural occurring deterioration can be explained as a single corrosion state and, therefore, multiple natural corrosion states must be considered.

4.2. The impact of sulfur

The tarnishing of Ag by S, which commonly produces a non-uniform film, can be attributed to several environmental considerations such as temperature, relative humidity, the amount of reduced S in the atmosphere (Pope *et al.*, 1968) and the state of the Ag surface (Yang *et al.*, 2007). Other factors such as the handling of the daguerreotype and perhaps physical disturbance by the owner (*e.g.* buffing with a cloth) would also impact the degree of corrosion on the surface. The placement of daguerreotypes within a sealed frame not only protects the surface from abrasions but also serves as a buffer from extreme variations in relative humidity; moisture content has been shown to significantly impact the corrosion rate on Ag (Pope *et al.*, 1968). However, alteration within the daguerreotype case is expected to occur, thereby creating a microenvironment where surface corrosion may be accelerated.

Possible sources of S corrosion include H_2S, SO_2, carbonyl sulfides (OCS) and organic sulfides (Reagor & Sinclair, 1981; Kim, 2003; Mao & Tian, 1995; Sinclair, 1982; Rice *et al.*, 1981); H_2S has been shown to be a source of Ag_2S at concentrations as low as 0.2 parts per billion (Huo *et al.*, 2016; Bennett *et al.*, 1969). In addition, while organic sulfides are generally present in low concentrations they have been shown to rapidly tarnish Ag surfaces especially in the presence of light (Graedel, 1992; Bennett *et al.*, 1969).

In urban environments, H_2S, SO_2 and OCS have the greatest reported concentrations of any likely tarnish sources. However, the reaction between Ag and SO_2 is relatively slow (Rice *et al.*, 1981; Franey *et al.*, 1985). While daguerreotypists often followed individuals on expeditions [*e.g.* the California Gold Rush of 1848 (Kennedy, 1981)], the majority of daguerreotype studios were found in city centres with their benefactors also residing in these urban environments. Therefore, any S species that would come into contact with the plate, which would occur prior to their placement behind a cover glass or when removed from their case, would be from an urban atmospheric environment (for instance H_2S and SO_2), while daguerreotypes produced in non-urban environments would primarily experience OCS (Bauer, 1988).

4.3. The impact of chlorine

Ag_2S and AgCl are the most common forms of Ag corrosion (Liang *et al.*, 2010; Watanabe *et al.*, 2006). Environmental Cl compounds contribute to the tarnishing of the daguerreotype surface; the rate of tarnish formation is concentration dependent (Rice *et al.*, 1981). Some AgCl on the daguerreotype surface may be residue from the sensitization step [equation (1)] (Ravines *et al.*, 2016*b*). Similar to the exposure step, any residual AgCl trapped within the Ag lattice may undergo reduction from UV exposure [equation (2)] to form Ag nanoparticles (Wan *et al.*, 2012). This has been noted to occur on daguerreotypes under natural and experimental conditions (Robinson & Vicenzi, 2015),

$$2\mathrm{Ag(s)} + \mathrm{Cl_2(g)} \rightarrow 2\mathrm{AgCl(s)}, \quad (1)$$

$$2\mathrm{AgCl(s)} + h\nu \rightarrow 2\mathrm{Ag(s)} + \mathrm{Cl_2(s)}. \quad (2)$$

Deterioration of the cover glass could also lead to the production of AgCl as a result of alkali ions in the cover glass matrix interacting with water vapour (Barger *et al.*, 1989).

4.4. Tarnish distribution

The differing distribution of Cl and S observed on both daguerreotypes may be the result of a variety of factors

including but not limited to: (1) differential exposure to the atmosphere, the concentration of which may vary significantly over time; (2) a large number of different chemically reactive sites that are influenced by particle size and/or distribution as well as surface defects, discontinuous gilding surface and differing degrees of amalgamation between Hg, Ag and Au; (3) possible effects of the cover glass and the microclimate that is created between the glass and the plate; (4) the migration of S and Cl compounds from the image particles to the vicinity from past physical or chemical treatments; (5) incomplete washing of the surface during preparation of the original daguerreotype; and (6) previous conservation effort(s) where a harmful treatment and/or an insufficient wash post-cleaning was performed. It is probable that the reactivity of the daguerreotype surface changes significantly from site to site and is one of the challenging problems associated with the analysis of these historical images.

4.5. Impact of Cu on corrosion formation

The daguerreotype plate is manufactured through a cold welding process. The end result is a Ag-coated Cu plate that is ∼0.4 mm thick with the Ag surface layer being ∼4 µm thick (Swan *et al.*, 1979); this would vary between producers. While the integration of the Cu backing improves the strength of the Ag plate (Butts, 1967), the migration of Cu to the surface via grain boundaries in the Ag layer has been suggested (Ravines *et al.*, 2016*a*). The Cu may then act as a catalyst for Ag corrosion or form deterioration compounds on the surface. However, there is no evidence in this study to support these processes.

4.6. Influence of Ag–Au alloy on corrosion compounds

Alloying with Au would also impact the probability and possible processes of corrosion. Despite Au's inert characteristics, when present in a Ag–Au alloy with a Au content of <50%, Au's corrosion and tarnish resistance is greatly reduced, which is the case for the daguerreotype's composition (Wright *et al.*, 1981). Kozachuk *et al.* (2017*a*) showed that the composition of the Ag–Au alloy in the shadow and midtone regions varied from the highlight regions, with a greater degree of alloying being observed in the shadow regions while a relatively greater amount of Au was observed on the surface in the highlight areas. The difference may depend on differential interaction with the gilding solution because of changes in surface area and/or possible diffusion of gold into the silver. Moreover, the number of phases present and the microstructure of the alloy will also impact the corrosion resistance of a material (Wright *et al.*, 1981).

5. Conclusions

The primary tarnish compounds were Ag_2S and AgCl and were found to be associated with high-density image-particle regions. These results are in agreement with the SEM–EDX analysis. XRF imaging showed that S and Cl possibly undergo different reaction pathways, an indication of a surface whose reactivity varies dramatically from place to place. This may be because of an artefact's original production, its past treatment(s) and/or handling. However, ambient environment over time is more likely to be the cause for surface degradation. Therefore, a combination of conservation treatments is most likely to be required when treating daguerreotypes. Future work will include the collection of XANES and localized XRF imaging of Hg that will be analyzed alongside a wide range of Hg standards.

Acknowledgements

This work was made possible through the generous collaboration with John McElhone of the Canadian Photography Institute at the National Gallery of Canada. Scanning electron microscopy energy-dispersive X-ray spectroscopy images were collected with the assistance of Todd Simpson, Western Nanofabrication. The technical assistance of the beamline staff at the Canadian Light Source, Saskatoon, Saskatchewan, Dr Yongfeng Hu and Dr Qunfeng Xiao, is acknowledged.

Funding information

Synchrotron experiments were performed at the Canadian Light Source, which is supported by the National Science and Engineering Research Council of Canada (NSERC), the National Research Council Canada (NRC), the Canadian Institutes of Health Research (CIHR) and the University of Saskatchewan. This research was supported by the NSERC (grant number TKS: DG, RGPIN-2014-04113), the Canadian Foundation for Innovation, Canada Research Chairs and the Ontario Ministry of Innovation. Further support for interdisciplinary research was provided by The Dean's Office at The University of Western Ontario, Faculty of Science.

References

Anglos, D., Melesanaki, K., Zafiropulos, V., Gresalfi, M. J. & Miller, J. C. (2002). *Appl. Spectrosc.* **56**, 423–432.
Arago, F. (1839). *Le Daguerréotype C. R. des Séances de L'Académie des Sciences*, pp. 250–267. Paris: Bachelier.
Barger, S. M., Krishnaswamy, S. V. & Messier, R. (1982*a*). *J. Am. Inst. Conserv.* **22**, 13–24.
Barger, S. M., Messier, R. & White, W. B. (1982*b*). *Photogr. Sci. Eng.* **26**, 285–291.
Barger, S. M., Smith, D. K. & White, W. B. (1989). *J. Mater. Sci.* **24**, 1343–1356.
Barger, S. M. & White, W. B. (1991). *The Daguerreotype: Nineteenth Century Technology and Modern Science.* Washington: Smithsonian Institution Press.
Bauer, R. (1988). *J. Spacecr. Rockets*, **25**, 439–440.
Bennett, H. E., Peck, R. L., Burge, D. K. & Bennett, J. M. (1969). *J. Appl. Phys.* **40**, 3351–3360.
Butts, A. (1967). *Silver Economics Metallurgy and Use*, pp. 123–136. Princeton: Van Nostrand and Co.
Centeno, S. A., Schulte, F., Kennedy, N. & Schrott, A. (2011). *Appl. Phys. A*, **105**, 55–63.
Da Silva, E., Robinson, M., Evans, C., Pejović-Milić, A. & Heyd, D. F. (2010). *J. Anal. At. Spectrom.* **25**, 654–661.
Franey, J. P., Kammlott, G. W. & Graedel, T. E. (1985). *Corros. Sci.* **25**, 133–143.
Graedel, T. E. (1992). *J. Electrochem. Soc.* **139**, 1963–1970.

Hogan, D. L., Golovlev, V. V., Gresalfi, M. J., Chaney, J. A., Feigerie, C. S., Miller, J. C., Romer, G. & Messier, P. (1999). *Appl. Spectrosc.* **53**, 1161–1168.
Hu, Y. F., Coulthard, I., Chevrier, D., Wright, G., Igarashi, R., Sitnikov, A., Yates, B. W., Hallin, E. L., Sham, T. K. & Reininger, R. (2010). *AIP Conf. Proc.* **1234**, 343–346.
Huo, Y., Fu, S.-W., Chen, Y.-L. & Lee, C. C. (2016). *J. Mater. Sci. Mater. Electron.* **27**, 10382–10392.
INCA (2006). *INCA Energy Operator Manual*, pp. 1–84. High Wycombe: Oxford Instruments Analytical.
Kennedy, M. (1981). *Calif. Hist.* **60**, 370–375.
Kim, H. (2003). *Mater. Corros.* **54**, 243–250.
Kozachuk, M. S., Martin, R. R., Sham, T. K., Robinson, M. & Nelson, A. J. (2017*a*). *Can. J. Chem.* **95**, 1156–1162.
Kozachuk, M. S., Sham, T. K., Martin, R. R., Robinson, M., Nelson, A. J. & Biesinger, M. C. (2017*b*). *Int. J. Conserv. Sci.* **8**, 675–684.
Lavédrine, B., Gandolfo, J.-P., McElhone, J. & Monod, S. (2009). *Photographs of the Past: Process and Preservation.* Los Angeles: Getty Conservation Institute.
Liang, D., Allen, H. C., Frankel, G. S., Chen, Z. Y., Kelly, R. G., Wu, Y. & Wyslouzil, B. E. (2010). *J. Electrochem. Soc.* **157**, C146–156.
Manceau, A. & Nagy, K. L. (2012). *Geochim. Cosmochim. Acta*, **99**, 206–223.
Mao, X. Y. & Tian, K. S. (1995). *Electroplat. Pollut. Contrib.* **15**, 8–12.
Marquis, E. A., Chen, Y., Kohanek, J., Dong, Y. & Centeno, S. A. (2015). *Corros. Sci.* **94**, 438–444.
Pope, D., Gibbens, H. R. & Moss, R. L. (1968). *Corros. Sci.* **8**, 883–887.
Ravel, B. (2009). *Athena User's Guide.* Chicago: The University of Chicago.
Ravel, B. & Newville, M. (2005). *J. Synchrotron Rad.* **12**, 537–541.
Ravines, P. (2010). *Am. Lab.* **42**, 20–25.
Ravines, P., Li, L., Chan, L. & McElroy, R. (2016*a*). *Nanoscience and Cultural Heritage*, edited by P. Dillman, L. Bellot-Gurlet & I. Nenner, pp. 123–158. Paris: Atlantis Press.
Ravines, P., Li, L. & McElroy, R. (2016*b*). *J. Imaging Sci. Technol.* **60**, 030504-1–030504-10.
Ravines, P., Wiegandt, R. & Wichern, C. M. (2008). *Surf. Eng.* **24**, 138–146.
Reagor, B. T. & Sinclair, J. D. (1981). *J. Electrochem. Soc.* **128**, 701–705.
Rice, D. W., Peterson, P., Rigby, E. B., Phipps, P. B. P., Cappell, R. J. & Tremoureux, R. (1981). *J. Electrochem. Soc.* **128**, 275–284.
Robinson, M. (2017). Dissertation. De Montfort University, Leicester, UK.
Robinson, M. & Vicenzi, E. P. (2015). *Top. Photogr. Preserv.* **16**, 187–205.
Sinclair, J. D. (1982). *J. Electrochem. Soc.* **129**, 33–40.
Solomon, D., Lehmann, J. & Martínez, C. E. (2003). *Soil Sci. Soc. Am. J.* **67**, 1721–1731.
Storme, P., Schalm, O. & Wiesinger, R. (2015). *Herit. Sci.* **3**, 1–15.
Swan, A., Fiori, C. E. & Heinrich, K. F. J. (1979). *Scan. Electron Microsc.* **1**, 411–424.
Wan, Y., Macha, E. N. & Kelly, R. G. (2012). *Corrosion*, **68**, 036001-1–036001-10.
Watanabe, M., Shinozaki, S., Toyoda, E., Asakura, K., Ichino, T., Kuwaki, N., Higashi, Y. & Tanaka, T. (2006). *Corrosion*, **62**, 243–250.
Webb, S. M., McNulty, I., Eyberger, C. & Lai, B. (2011). *AIP Conf. Proc.* **196**, 196–199.
Wright, D. C., German, R. M. & Gallant, R. F. (1981). *J. Dent. Res.* **60**, 809–814.
Yang, C. J., Liang, C. H. & Liu, X. (2007). *Anti-Corrosion Methods Mater.* **54**, 21–26.